2014 M=6.0 South Napa earthquake triggered widespread aftershocks and stressed several major faults and exotic fault clusters

Shinji Toda[1] and Ross S. Stein[2]

[1] International Research Institute of Disaster Science (IRIDeS),
Tohoku University, Sendai, Japan

[2] U.S. Geological Survey
Menlo Park, California
345 Middlefield Road
Menlo Park, California 94025

Corresponding author:
Shinji Toda
International Research Institute of Disaster Science (IRIDeS),
Tohoku University, Sendai, Japan
Aoba, 468-1, Aoba, Sendai 980-0845, Japan
E-mail: toda@irides.tohoku.ac.jp
Phone: +81-22-752-2062

INTRODUCTION

The strongest San Francisco Bay area earthquake since the 1989 M=7.0 Loma Prieta shock struck south of Napa, California, on August 24, 2014. Field mapping revealed (Dawson *et al.*, 2014; EERI, 2014; Brocher *et al.*, 2015) and seismic and geodetic source inversions (Barnhart *et al.*, 2015; Dreger *et al.*, 2015; Wei *et al.*, 2015) confirm that a 15-km-long NW-trending section of the West Napa Valley fault ruptured in the earthquake, the first indisputable surface-rupturing earthquake in the Bay area since 1906. This event, along with other smaller earthquakes on the Calaveras and Hayward faults over the past 3-4 decades, may indicate that the Bay area region is emerging from the stress shadow of the 1906 M=7.8 San Francisco earthquake (Harris and Simpson, 1998; Pollitz *et al.*, 2004). In the broader Bay area, there have been 113 M≥4.1 shocks during the 36-yr period since 1979, nine with M≥5.5 (M=4.1 is the magnitude of completeness). In the preceding 36 yr, there were 81 M≥4.1 shocks, only two with M≥5.5. Most of the events M≥4.1 since about 1979 are concentrated in a corridor extending north from the 1989 Loma Prieta aftershock zone through the Calaveras, Greenville, Green Valley, Napa, and Rogers Creek faults east of the Bay (Fig. 1a). This corridor roughly coincides with the 1906 stress shadow that is being eroded away by more than a century of stress re-accumulation. The Napa event, as well as the surrounding faults on which we calculate the resulting hazard increases, all lie within this reawakening zone.

Despite a very low aftershock productivity, the South Napa M=6 earthquake has a high proportion of remote aftershocks. We therefore explore how stress imparted by the 2014 mainshock changed the surrounding seismicity, and we estimate the influence of the South Napa shock on stress and future seismic hazard on the densely populated Bay Area faults nearby. We find that, in addition to the sections of the West Napa fault to the north and south of the rupture, the Concord-Green Valley fault experienced a transient seismicity rate increase, and we calculate it sustained a Coulomb stress increase that raises the likelihood of M≥7 Green Valley ruptures by about 3% for the next several decades. A 5-km-long echelon at the junction of the Rodgers Creek and Hayward faults also received a calculated 0.5-bar stress increase and a seismicity rate jump.

AFTERSHOCK PRODUCTIVITY AND SEISMICITY RATE CHANGE

The South Napa aftershock productivity is very low relative to other M~6.0 California earthquakes (Brocher *et al.*, 2015), which we probe in Fig. 2 and Table 2. But although the aftershock rate is a full order of magnitude lower than the 1992 M=6.1 Joshua Tree event, the South Napa mainshock triggered far more off-fault aftershocks than did the 2004 M=6.0 Parkfield earthquake (Bakun *et al.*, 2005). These remote aftershocks provide a further basis for testing the Coulomb calculations.

We use the ANSS (Advanced National Seismic System) composite catalog and compare the first two months of post-mainshock seismicity with the preceding 5 years in Fig. 3b and Fig. 3c, assuming that the detection level was constant during this period (Fig. S1). Because of the low background rate and the short post-mainshock time period, it is impossible to measure seismicity rate decreases, but increases extending ~25 km beyond the ends of the South Napa rupture (marked '1' in Fig. 3c), as well as along several portions of the Rodgers Creek and Green Valley faults (marked 2-5 in Fig. 4c) are evident. More abundant seismicity rate increases to the north of the rupture could be a directivity effect of its northward propagation (Brocher *et al.*, 2015; Dreger *et al.*, 2015). Comparison of Fig. 3a with Fig. 3c shows that the shear stress is calculated to have increased on the nodal planes of these remote aftershocks.

COULOMB STRESS CHANGE ANALYSIS

We first calculate the Coulomb stress change caused by the South Napa earthquake in the surrounding crust and on the adjacent faults in an elastic half-space (Okada, 1992). We use the variable slip model of Barnhart *et al.* (2015) inverted from 56 continuous GPS time series, and from surface displacements from a coseismic interferogram by the JPL/ARIA group. The rupture source is roughly 15 km long and 10 km wide, striking 341° and dipping 80°E. The rake, or slip direction, is fixed to 178° (right-lateral) for all sub-patches. Most of the slip, up to 1.2 m, is concentrated on an 8-km-long central section, between 3-7 km deep. We note that the model we used resembles the 2-plane source of Wei *et al.* (2015), which also dips to the east and has the same overall strike and location. The source of Dreger *et al.* (2015) dips 82°W, but is otherwise similar in seismic moment and extent, although it has significant non-horizontal rake at the ends. All source inversions concur that rapid posteismic slip increased the net moment to an equivalent M=6.1; the Barnhart *et al.* (2015) source that

we use includes 3 days of post-seismic slip in the GPS time series and a single interferogram. Since the post seismic slip also contributes to the stress transfer, this inclusion is permissible.

We resolve the Coulomb stress changes on three types of 'receivers' (faults in the surrounding crust that are subjected to stress changes caused by the South Napa source) to assess whether fault slip is promoted or inhibited. Each approach has its own intrinsic advantages and shortcomings; none takes precedence:

1) The first are vertical strike-slip receivers that, for a given fault friction coefficient, are optimally oriented with respect to the combined regional stress and the Napa stress changes (King *et al.*, 1994). Here we do not use mapped faults but instead attempt to capture the role of small faults. We use this approach to determine if stress increases are correlated with the distribution of aftershocks, since aftershocks need not occur on the major mapped faults. The implicit assumption in optimally oriented Coulomb stress is that small faults with a range of orientations exist everywhere in the crust; the faults with the optimum geometry (on which the Coulomb stress increase is most positive), will be most likely to host aftershocks (Fig. 1b). In Fig. S2, we explore the impact of the full range of principal stress azimuths and fault friction on this result.
2) Next, we resolve the Coulomb stress changes on the mapped active faults within 50 km (about three rupture dimensions from the source, beyond which the stress changes are negligible, <0.05 bar), using the known or inferred fault rakes and dips compiled into the UCERF3 fault model (Field *et al.*, 2014). The goal for this calculation is to estimate the hazard changes on faults thought to be capable of M≥7 shocks (Fig. 4). In Fig. S3, the full range of friction coefficients is explored.
3) Finally, we calculate the Coulomb stress change on the nodal planes of focal mechanisms for events having occurred during 15 years before and two months after the South Napa earthquake in and around the 2014 source fault (lon.: -122.7° to -122.0°, lat.: 37.9° to 38.6°). The nodal planes of shocks that struck before the Napa quake (Fig. 5b and Fig. S4a-c) serve as proxies for small active faults, while the nodal planes of Napa aftershocks (Fig. 5c and Fig. S4d) reveal which structures became active after the mainshock.

Remote aftershocks concentrate in the stress-trigger lobes

There are three elements needed for the calculation of the stress imparted to optimally oriented strike-slip faults (receiver type 1 described above): The receiver fault dip and rake,

which we take to be vertical and right-lateral; the fault friction coefficient, which we assume to be 0.4; and the regional stress tensor, which we simplify with an S_{Hmax} orientation and a differential stress compatible with strike-slip faulting. We take S_{Hmax} from Townend and Zoback (2004), who found a range of 22°-46° (reckoned clockwise from North) for the Bay area. We thus assume the σ_1 direction of the regional stress is 34° and its amplitude is 100 bar that is comparable to a typical earthquake stress drop (e.g., King *et al*., 1994). We set σ_3 to be horizontal and perpendicular to σ_1, with σ_2 vertical (Table 1). Close to the source rupture, the stress imparted by the earthquake and the regional stress have roughly the same magnitude, and so the optimal planes rotate. Far from the source, the optimal planes are essentially fixed by the regional stress azimuth and the friction coefficient.

We find that about 90% of the off-fault aftershocks that struck during the first 53 days occurred where the calculated Coulomb stress increased (Fig. 1b). Many aftershocks occurred in the northern and southern stress increase lobes beyond the edges of the source fault, and about 10 events occurred in the western and eastern side lobes. The greatest number of shocks in one of the side lobes locates near the Green Valley fault, a finding we first presented in Parsons *et al.* (2014).

Several major active faults were stressed

We represent the faults by contiguous rectangular patches (Fig. 4). For the Barnhart *et al.* (2015) rupture source, and for the adjacent portions of the West Napa fault, the patches are 4 km long x 2 km deep. For other faults within 20 km of the source, the patches are larger (3-5-km long by 4.5-5-km deep), and for faults at greater distance, fault patches are <10 km along strike and 10-15 km deep.

Our results indicate that portions of the Green Valley, West Napa, Contra Costa, and Franklin faults were brought up to 0.5 bar closer to failure; the increase was >0.2 bar for a length of 15 km along strike. In addition, a 6-km long echelon between the Rodgers Creek and Hayward faults was also brought >0.5 bar closer to failure. Parsons *et al.* (2014) and Barnhart *et al.* (2014) reported similar, independent findings. Parsons *et al.* examined two values of fault friction at a single depth (0.2 and 0.4; which we also do in Fig. S3), and Barnhart *et al.* examined two source fault dips (80°E and 76°W).

Exotic aftershock focal mechanisms reveal a heterogeneous stress field

The Coulomb stresses on the two nodal planes of a focal mechanism are different; to avoid this ambiguity, we resolve the imparted shear stress only, equivalent to assuming friction of zero. We find that the majority (~80%) of the aftershock focal mechanisms more than 4 km of the source fault are calculated to have experienced shear stress increases. (Figure 3a). The stress changes closer to the source are sensitive to details in the slip model that may be artifacts of the slip inversion procedure (i.e. over-simplified fault geometry, rake, and inversion regularization).

That a majority of mechanisms in Fig. 3a are positively stressed does not, in itself mean that the mainshock stress promoted the aftershocks, if this same 80% percentage might be found among the pre-mainshock, or background, shocks. To test causality, we perform the same source-fault stress transfer calculation to the mechanisms during the preceding 15 years (Fig. S4), and find that 40% are positive before the mainshock. The factor or 2 increase in positively-stressed mechanisms means that the aftershocks were most likely promoted.

The Green Valley fault slips at 6±1 mm/yr, about half of which occurs as creep (Lienkaemper *et al*., 2014). Paleoseismic investigation suggests a ~200-yr recurrence interval for M~7 shocks on the fault, and ~400 yr has elapsed since the last large earthquake (Lienkaemper *et al.*, 2013). The fault also poses a substantial risk, since it bisects the city of Concord, with 200,000 residents. Thus, perhaps the most important remote earthquake cluster lies near the Green Valley fault (the eastern stress lobe in Fig. 1b, and the highlighted rectangle in Fig. 3a).

The Green Valley seismicity cluster began 2-3 days after the mainshock, and contains 15 aftershocks with focal mechanisms. As can be seen in Fig. 1b, only a quarter of the events occur in the stress-increase lobe for optimally-oriented faults in the assumed regional stress field, while three-quarters strike in the stress decrease lobe. Yet, when the shear stress is resolved on the nodal planes of the focal mechanisms along the Green Valley fault, the proportion of positively stressed mechanisms rises from about 10% before the mainshock (Fig. 5b) to 80% afterwards (Fig. 5c), consistent with the Coulomb hypothesis despite their occurrence in the stress shadow for optimally oriented strike-slip faults. As before, the pre-mainshock period serves as the control and the post-mainshock period as the test set; the difference between the two sets is what matters. Hypocenters of the pre- and post-mainshock

clusters in the boxed area of Fig. 5 are remarkably close to each other; they lie within 2-3 km (the mean depth of the pre- and post-mainshock clusters is 9.2 and 7.5 km, respectively).

The pre-mainshock mechanisms are consistent with right-lateral slip on the Green Valley or smaller subsidiary faults in our inferred regional stress system (compare the assumed stress field in Fig. 5a with that inverted in Fig. 5d), but the mechanisms activated after the South Napa shock (Fig. 5c and Fig. 5e) are not. After the mainshock, the σ_1 inferred from the focal mechanisms is oriented nearly perpendicular to the Green Valley fault (Fig. 5e), so these events most likely activate a different set of nearby faults. The stress tensor inversions are simplified in the inset boxes in Fig. 5d-e.

At the site of the aftershock cluster, the Green Valley fault and optimally-oriented strike-slip faults are inhibited from failure, but reverse faults parallel to the Green Valley are promoted by ~1 bar (Fig. 5f). So, to explain the 65° clockwise change in the inferred σ_1 direction, there must be a nest of faults with many orientations, so that a different set of faults could activate in response to the stress change. This can only occur if the tectonic stress is much more heterogeneous than we have assumed, because only in a heterogeneous stress field could both fault populations be active when the earthquake stress change is only 1 bar. A similar Coulomb finding was reported by Toda *et al.* (2011) for the M=9.0 Tohoku-Oki megathrust earthquake, whose shallow aftershocks were largely normal events. Stress heterogeneity was proposed as a widespread phenomenon by Smith and Dietrich (2010), and further explored by Smith and Heaton (2011).

The focal mechanism analysis reveals why, while widely practiced, resolving the stress on assumed optimal orientations (Fig. 1b), or on major active faults (Fig. 4), can be misleading: Even though the burst of aftershocks lies within 2 km of the Green Valley fault, they are unlikely to have anything to do with the Green Valley fault, and their orientation is optimal only for a unique and quite local tectonic stress condition.

HEIGHTENED PROBABILITY OF GREEN VALLEY FAULT RUPTURE

We next seek to estimate how the South Napa earthquake altered the likelihood of failure on the Green Valley fault. As evident in Fig. 4, a 15-km-long section of the fault was brought <1.0 bar closer to failure, but the adjacent 20-km-long section to the south was inhibited from failure by up to 2.0 bar. The net effect over the 35-km-long section is negative (-0.5 bar). So, what is important, the local increase or the net decrease?

The stress transfer from the South Napa earthquake to the Green Valley fault, resembles the transfer from the 1992 M=7.3 Landers shock to the Lavic Lake fault—which subsequently ruptured in the 1999 M=7.1 Hector Mine shock (Fig. 1c). Further, the Landers earthquake also produced remote aftershocks near, but not on, the Lavic Lake fault with a non-parallel focal mechanisms (Hauksson *et al.*, 2002), and so these cases are remarkably similar. Another example is the 1997 M=6.5 and 6.3 Kagoshima, Japan, earthquakes (Toda and Stein, 2003); in both the California and Japanese sequences, the second earthquake nucleated on or near a promoted section of the fault, and then propagated into or through inhibited sections. These examples suggest that under some circumstances, what counts is the peak stress increase, even if it is isolated.

So, use the calculated 0.6-bar Coulomb stress imparted by the Napa mainshock, and the seismicity rate equation of Dieterich (1994) to calculate the expected response of seismicity to the stress jump. We then calculate the time-dependent probability of a surface-cutting earthquake on the Green Valley fault unperturbed by the South Napa event, using the paleoseismic occurrence information from Lienkaemper *et al.* (2013): a 250-yr interevent time with a 0.6 coefficient of variation, and 400 yr since the last event. This yields a 30-yr probability of 18.5%.

This rate/state Coulomb calculation is sensitive to the assumed aftershock duration and a fault constitutive parameter on the Green Valley fault, creating considerable uncertainty. Aftershock duration is the time until the seismicity rate returns to the pre-mainshock rate; it can be measured on the source fault or on a nearby receiver. In general, we have found that aftershock durations grow with distance from the San Andreas, probably because the stressing rate declines with distance (Table 3). On the South Napa fault, we project the aftershock duration to be 7-10 yr (Fig. S5). We have generally inferred the fault constitutive parameter times the normal stress, $A\sigma$, to be about 0.5 bar (Toda and Stein, 2002; Toda *et al.*, 2005). The fault stressing rate is proportional to slip rate for isolated faults of the same length; rates of 0.05-0.5 bar/yr bracket the likely range of this fault. The resulting range of probabilities is shown in Fig. 6, of which we consider the blue curve (a 5-yr aftershock duration and 0.1 bar/yr stressing rate) to be the best or median estimate. If so, the South Napa shock will have elevated the M≥7 probability modestly for up to several decades.

CONCLUSIONS

Despite a very low aftershock productivity, the South Napa M=6 earthquake has a high proportion of remote aftershocks that occur up to 25 km from the rupture. Coulomb stress calculations indicate that these aftershocks were generally promoted by the stress imparted by the mainshock, even when the faults on which these quakes struck differed substantially in orientation from the major surface faults, or those expected to be optimally oriented in a simple uniform tectonic stress field. Subsequent large earthquakes on the West Napa fault to the north, the Franklin and Contra Costa faults to the south, and the Green Valley fault to the east, would appear possible because 15-km or longer sections of all of these faults received a calculated stress increase of more than 0.5 bar. Because paleoseismic evidence indicates that surface-cutting (M>6.5) ruptures on the Green Valley fault have occurred every 250±150 yr, and 400 yr has elapsed since the last event, this urban fault bears special scrutiny.

Furnishing a time-dependent probabilistic rupture forecast on the Green Valley fault is uncertain because the northern portion received a calculated stress increase while the central portion a decrease. But the resemblance between the stress imparted to the Green Valley fault by the South Napa mainshock, and the stress imparted to the Lavic Lake fault by the Landers earthquake, encourages us to base our calculation on the 15-km-long patch of the Green Valley fault brought 0.6 bar closer to failure. This results in the 30-yr earthquake probability rising from 18.5% to as high as 22-25%, which is forecast to decay back to 19% over the next 5-20 years. Further monitoring of seismicity and strain on the Green Valley fault would seem prudent, given this modest and uncertain hazard increase.

ACKNOWLEDGEMENTS

We thank Tom Parsons, Andrea Llenos, Jim Lienkaemper, Tim Dawson, and Volkan Sevilgen for insights and discussion. We are also grateful to William Barnhart and Deborah Smith for their thoughtful and careful reviews.

REFERENCES

Bakun, W. H. , B. Aagaard, B. Dost, W. L. Ellsworth, J. L. Hardebeck, R. A. Harris, C. Ji, M. J. S. Johnston, J. Langbein, J. J. Lienkaemper, A. J. Michael, J. R. Murray, R. M. Nadeau, P. A. Reasenberg, M. S. Reichle, E. A. Roeloffs, A. Shakal, R. W. Simpson and F. Waldhauser (2005). Implications for prediction and hazard assessment from the 2004 Parkfield, earthquake, *Nature*, **437**, doi:10.1038/nature04067.

Barnhart, W. D., J. R. Murray, S.-H. Yun, J. L. Svarc, S. V. Samsonov, E. J. Fielding, B. A. Brooks, and P. Milillo (2015). Geodetic Constraints on the 2014 M 6.0 South Napa Earthquake, *Seismol. Res. Lett.,* **86**, 344-354, doi: 10.1785/0220140210.

Brocher, T. M., A. S. Baltay, J. L. Hardebeck, F. F. Pollitz, J. R. Murray, A. L. Llenos, D. P. Schwartz, J. L. Blair, D. J. Ponti, J. J. Lienkaemper, V. E. Langenheim, T. E. Dawson, K. W. Hudnut, D. R. Shelly, D. S. Dreger, J. Boatwright, B. T. Aagaard, D. J. Wald, R. M. Allen, W. D. Barnhart, K. L. Knudsen, B. A. Brooks, and K. M. Scharer (2015). The Mw 6.0 24 August 2014 South Napa Earthquake, *Seismol. Res. Lett.,* **86**, 309-326, doi: 10.1785/0220150004.

Dawson, T., K. Kelson, J. Wesling, K. Hudnut, and D. Ponti (2014). Section 3: Surface Fault Rupture Associated with the M6.0 South Napa Earthquake of August 24, 2014, in August 24, 2014 South Napa, California Earthquake, *Report for Web Dissemination, GEER Association,* Rep. No. GEER-037, http://www.geerassociation.org/GEER_Post%20EQ%20Reports/SouthNapa_2014/index.html

Dieterich, J. (1994). A constitutive law for rate of earthquake production and its application to earthquake clustering, *J. Geophys. Res*., **99**, 2601-2618.

Dreger, D. S., M. H. Huang, A. Rodgers, T. Taira and K. Wooddell (2015). Kinematic Finite Source Model for the 24 August 2014 South Napa, California, Earthquake from Joint Inversion of Seismic, GPS, and InSAR Data, *Seismol. Res. Lett.,* **86**, 327-334, doi: 10.1785/0220140244.

EERI (2014). M 6.0 South Napa Earthquake of August 24, 2014, *EERI Special Earthquake Report* (October 2014), 27 p., http://www.eqclearinghouse.org/2014-08-24-south-napa/preliminary-reports.

311 Felzer, K. R., T. W. Becker, R. E. Abercrombie, G. Ekstrom, and J. R. Rice (2002).
312 Triggering of the 1999 Mw 7.1 Hector Mine earthquake by aftershocks of the 1992 Mw
313 7.3 Landers earthquake, *J. Geophys. Res*., **107**, 2190, doi:10.1029/2001JB000911.

314 Felzer, K. R. (2013). Appendix K—The UCERF3 Earthquake Catalog, in Field, E.H., et al.,
315 Uniform California Earthquake Rupture Forecast, Version 3 (UCERF3)—The Time-
316 Independent Model: *U.S. Geol. Surv. Open-File Rep*. **2013–1165**,
317 http://pubs.usgs.gov/of/2013/1165/.

318 Field, E. H., R. J. Arrowsmith, G. P. Biasi, P. Bird, T. E. Dawson, K. R. Felzer, D. D.
319 Jackson, J. M. Johnson, T. H. Jordan, C. Madden, A. J. Michael, K. R. Milner, M. T. Page,
320 T. Parsons, P. M. Powers, B. E. Shaw, W. R. Thatcher, R. J. Weldon II, and Y. Zeng
321 (2014). Uniform California Earthquake Rupture Forecast, version 3 (UCERF3) - The time-
322 independent model, *Bull. Seismol. Soc. Amer*., **104**, 1122-1180, doi: 10.1785/0120130164.

323 Harris, R. A., and R. W. Simpson (1998). Suppression of large earthquakes by stress
324 shadows: A comparison of Coulomb and rate-and-state failure, *J. Geophys. Res.*, **103**,
325 24439-24451.

326 Hauksson, E., L. M. Jones, and K. Hutton (2002). The 1999 Mw 7.1 Hector Mine, California,
327 earthquake sequence: Complex conjugate strike-slip faulting, *Bull. Seismol. Soc. Amer*.,
328 **92**, 1154-1170.

329 Hudnut, K. W., T. M. Brocher, C. S. Prentice, J. Boatwright, B. A. Brooks, B. T. Aagaard, J.
330 L. Blair, J. Fletcher, J. E. Erdem, C. W. Wicks, J. R. Murray, F. F. Pollitz, J. Langbein, J.
331 Svarc, D. P. Schwartz, D. J. Ponti, S. Hecker, S. DeLong, C. Rosa, B. Jones, R. Lamb, A.
332 Rosinski, T. P. McCrink, T. E. Dawson, G. Seitz, R. S. Rubin, C. Glennie, D. Hauser, T.
333 Ericksen, D. Mardock, D. F. Hoirup, and J. D. Bray (2014). Key recovery factors for the
334 August 24, 2014, South Napa earthquake, *U.S. Geological Survey Open-File Report,*
335 **2014–1249**, 51 p., http://dx.doi.org/10.3133/ofr20141249.

336 King, G. C. P., R. S. Stein, and J. Lin (1994). Static stress changes and the triggering of
337 earthquakes, *Bull. Seismol. Soc. Amer.,* **84***,* 935-953.

338 Lienkaemper, J. J., J. N. Baldwin, R. Turner, R. R. Sickler, and J. Brown (2013). A record of
339 large earthquakes during the past two millennia on the southern Green Valley fault,
340 California, *Bull. Seismol. Soc. Amer*., **103**, 2386-2403, doi: 10.1785/0120120198.

341 Lienkaemper, J. J., F. S. McFarland, R. W. Simpson, and S. J. Caskey (2014). Using surface
342 creep rate to infer fraction locked for sections of the San Andreas fault system in northern

California from alignment array and GPS data, *Bull. Seismol. Soc. Amer*., **104**, 3094-3114, doi: 10.1785/0120140117.

Martinez-Garzon, P., G. Kwiatek, M. Ickrath, and M. Bohnhoff, MSATSI: A MATLAB package for stress inversion combining solid classic methodology, a new simplified user-handling, and a visualization tool, *Seismol. Res. Lett*., **85**, 896-903, doi:10.1785/0220130189.

Okada, Y. (1992). Internal deformation due to shear and tensile faults in a half-space, *Bull. Seism. Soc. Amer*., **82**, 1018-1040.

Parsons, T., S. Toda, R. S. Stein, A. Barka, and J. H. Dieterich (2000). Heightened odds of large earthquakes near Istanbul: An interaction-based probability calculation, *Science*, **288**, 661-665.

Parsons, T., and D. S. Dreger (2000). Static-stress impact of the 1992 Landers earthquake sequence on nucleation and slip at the site of the 1999 M=7.1 Hector Mine earthquake, southern California, *Geophys. Res. Lett*., **27**, 1949-1952.

Parsons, T., M. Segou, V. Sevilgen, K. Milner, E. Field, S. Toda, and R. S. Stein (2014). Stress-based aftershock forecasts made within 24 h postmain shock: Expected north San Francisco Bay area seismicity changes after the 2014 $M = 6.0$ West Napa earthquake, *Geophys. Res. Lett.*, **41**, 8792–8799, doi:10.1002/2014GL062379.

Pollitz, F., W. H. Bakun, and M. Nyst (2004). A physical model for strain accumulation in the San Francisco Bay region: Stress evolution since 1838, *J. Geophys. Res*., **109**, B11408, doi:10.1029/2004JB003003.

Smith, D. E., and J. Dieterich (2010). Aftershock sequences modeled with 3-D stress heterogeneity and rate-state seismicity equations: Implications for crustal stress estimation, *Pure Appl. Geophys.,* **167**, 1067–1085, do 10.1007/s00024-010-0093-1.

Smith, D. E., and T. H. Heaton (2011). Models of stochastic, spatially varying stress in the crust compatible with focal-mechanism data, and how stress inversions can be biased toward the stress rate, *Bull. Seism. Soc. Amer*., **101**, 1396-1421, doi:10.1785/0120100058.

Stein, R. S., A. A. Barka, and J. H. Dieterich (1997). Progressive failure on the North Anatolian fault since 1939 by earthquake stress triggering, *Geophys. J. Int*., **128**, 594-604.

Stein, R. S. (1999). The role of stress transfer in earthquake occurrence, *Nature*, **402**, 605–609, doi:10.1038/45144.

Toda, S., R. S. Stein, P. A. Reasenberg, and J. H. Dieterich (1998). Stress transferred by the Mw=6.5 Kobe, Japan, shock: Effect on aftershocks and future earthquake probabilities, *J. Geophys. Res*., **103**, 24,543-24,565.

Toda S., and R. S. Stein (2002). Response of the San Andreas fault to the 1983 Coalinga-Nuñez Earthquakes: An application of interaction-based probabilities for Parkfield, *J. Geophys. Res.,* **107**, 10.1029/2001JB000172.

Toda, S. and R. S. Stein (2003). Toggling of seismicity by the 1997 Kagoshima earthquake couplet: A demonstration of time-dependent stress transfer. *J. Geophys. Res.* **108**, 2567, doi:10.1029/2003JB002527.

Toda,S., R. S. Stein, K. Richards-Dinger, and S. B. Bozkurt (2005). Forecasting the evolution of seismicity in southern California: Animations built on earthquake stress transfer, *J. Geophys. Res*., **110**, B05S16, doi:10.1029/2004JB003415.

Toda,S., R. S. Stein and J. Lin (2011). Widespread seismicity excitation throughout central Japan following the 2011 M=9.0 Tohoku earthquake, and its interpretation by Coulomb stress transfer, *Geophys. Res. Lett.*, **38**, L00G03, doi:10.1029/2011GL047834.

Townend, J., and M. D. Zoback (2004). Regional tectonic stress near the San Andreas fault in central and southern California, *Geophys. Res. Lett*., **31**, L15S11, doi:10.1029/2003GL018918.

U.S. Geological Survey (2006). Quaternary fault and fold database for the United States, accessed DATE, from USGS web site: http//earthquakes.usgs.gov/regional/qfaults/.

Wei, S., S. Barbot, R. Graves, J. J. Lienkaemper, T. Wang, K. Hudnut, Y. Fu, and D. Helmberger (2015). The 2014 Mw 6.1 South Napa Earthquake: A Unilateral Rupture with Shallow Asperity and Rapid Afterslip, *Seismol. Res. Lett.,* **86**, 344-354, doi: 10.1785/0220140249

Woessner, J., and S. Wiemer (2005). Assessing the quality of earthquake catalogues: Estimating the magnitude of completeness and its uncertainty, *Bull. Seism. Soc. Amer*., **95**, 684-698.

Wiemer, S. (2001). A software package to analyse seismicity: ZMAP, *Seismol. Res. Lett*., **72**, 373-382.

Figure Captions

Fig. 1. (a) Moderate earthquakes during the past 36 yr in the San Francisco Bay area show an active corridor extending from Loma Prieta to the East Bay faults, of which the 2014 South Napa earthquake is only the most recent part. The Bay area is complete for M≥4.1 since 1942 (Felzer, 2013). (b) Maximum Coulomb stress change, using the Barnhart *et al.* (2015) source, on optimally oriented strike-slip faults at depths from 5 to 15 km. The regional stress field is assumed as shown in Table 1, and the coefficient of fault friction is set to be 0.4. Black lines denote the surface traces of the late Quaternary faults, younger than 130,000 years compiled by the USGS (2006). All recorded aftershocks during the first 53 days are plotted (24 August-16 October 2014). (c) A calculation from King *et al.* (1994) for the 1992 M=7.3 Landers earthquake bears a resemblance to the South Napa source-Green Valley fault configuration.

Fig. 2. Aftershock productivity and decay for three 6.0≤M≤6.1 California mainshocks. The areas from which the earthquakes were extracted is given in Table 2; each uses 60 days. It is evident that while they all have about the same temporal decay slope (p~1), the South Napa quake has a much lower productivity than the others.

Fig. 3. (a) Shear stress change resolved on aftershocks of the South Napa mainshcok, with the area of Fig. 5 identified. (b) Seismicity in the first two months after the mainshock. (c) The seismicity rate change associated with the mainshock, formed by the ratio of the rate during the first two months after the mainshock to the preceding 5 yr. Areas for which the rate change is undefined (principally because of the absence of earthquakes during either period) are grey. In addition, the post-mainshock period is too short to identify seismicity rate decreases. Salient off-fault rate increases are numbered.

Fig. 4. Coulomb stress change resolved on the Bay Area faults of the Uniform California Earthquake Rupture Forecast version 3 (UCERF3, Field *et al*., 2013). The Green Valley, West Napa, Contra-Costa, and Franklin faults are split into 3-5-km long by 4.5-5-km wide sub-patches and stress is calculated on the center of each sub-patch. For these faults there is an expanded view at right Colors saturate at ±0.5 bar.

Fig. 5. Mainshock-induced stress and focal mechanism changes near the Green Valley fault. (a) Our assumed tectonic stress, from Townend and Zoback (2004), drives the right-

lateral Green Valley fault. (b) Pre-mainshock focal mechanisms are consistent with the stress field in (a). After the mainshock, a larger percentage of mechanisms were promoted; here (b) is the control set and (c) is the test set. (d) The principal stress axes for the pre-mainshock period, 2009-2013, derived from 2,000 bootstrap resamplings using the MSATSI software (Martinez-Garzon *et al.,* 2014), match the assumed principal stress in (a); *R* is relative stress magnitude. (Only 12 mechanisms are available during the post South Napa period. Since the minimum number the software accepts is 20 seismic events, we simply doubled the original data to 24 events before resampling.) The stereo nets projected onto the lower hemisphere are simplified in the inset boxes. (e) For the post-mainshock mechanisms, the inferred principal stress axes are oriented ~65° clockwise. (f) The mechanisms in (c) are promoted by the stress imparted by the mainshock. (Additional pre-mainshock mechanisms are shown in Fig. S4.)

Fig. 6. Calculated 30-yr probabilities of a surface-rupturing earthquake on southern Green Valley fault as a function of time. The probability jump followed by a decaying probability is caused by the sudden stress change associated with the M=6.0 South Napa earthquake. The inter-event time, elapsed time, and coefficient of variation are based on geologic data of Lienkaemper *et al.* (2013). Three different aftershock durations, t_a, are assigned with the range of the estimates in Table 3; tau-dot is the fault stressing rate.

Table 1. Regional stress tensor used for Coulomb stress change on optimally oriented strike-slip faults in Fig. 1b.

	Azimuth (°)	Plunge (°)	Magnitude (bar)
$\sigma 1$	34	0	100
$\sigma 2$	34	90	30
$\sigma 3$	124	0	0

Table 2. Comparison of 60-day aftershock productivity between the three M~6 strike-slip, California earthquakes, in Fig. 2.

Mainshock	M	Number of M≥1.8	Number of M≥4.0	Maximum aftershock magnitude	Search area (lon./lat., polygon)
2014 South Napa	6.0	64	0	3.9	-122.700°/38.600°, -122.000°/38.600°, -122.000°/37.900°, -122.700°/37.900°
2004 Parkfield	6.0	548	9	5.0	-120.729°/36.066°, -120.617°/36.140°, -120.189°/35.758°, -120.306°/ 35.673°, -120.730°/36.066°
1992 Joshua Tree	6.1	3108	19	5.0	-116.500°/34.250°, -116.000°/34.250°, -116.000°/33.800°, -116.500°/33.800°

Table 3. Estimated aftershock durations for California earthquakes

Mainshock and Evaluated Fault	Aftershock duration (yr)	Distance from San Andreas fault (km)	Source of Estimate
Parkfied, creep & transition sections	0.5-3.0	0	Toda and Stein (2002)
Parkfield, 1966 locked section	3-10	0	Toda and Stein (2002)
2004 M = 6.0 Parkfield, section	2	0	This study
1992 M = 6.5 Big Bear fault	7	10-20	Toda & Stein (2005)
1987 M = 6.6 Superstition Hills fault	15	20-30	Toda & Stein (2005)
1989 M=6.9 Loma Prieta on San Gregorio f.	5-15	30-40	Stein (1999)
2014 M = 6.0 on West Napa fault	7-11	40-50	This study
1989 M=6.9 Loma Prieta on Hayward fault	7-11	40-50	Stein (1999)
1992 M = 7.3 Landers on Landers fault	25-50	50-70	Toda and Stein (2005)
1999 M = 7.1 Hector Mine, Lavic Lake fault	66	70-80	Toda and Stein (2005)
1995 M = 5.8 Ridgecrest on ECSZ faults	17-30	140	Toda and Stein (2005)

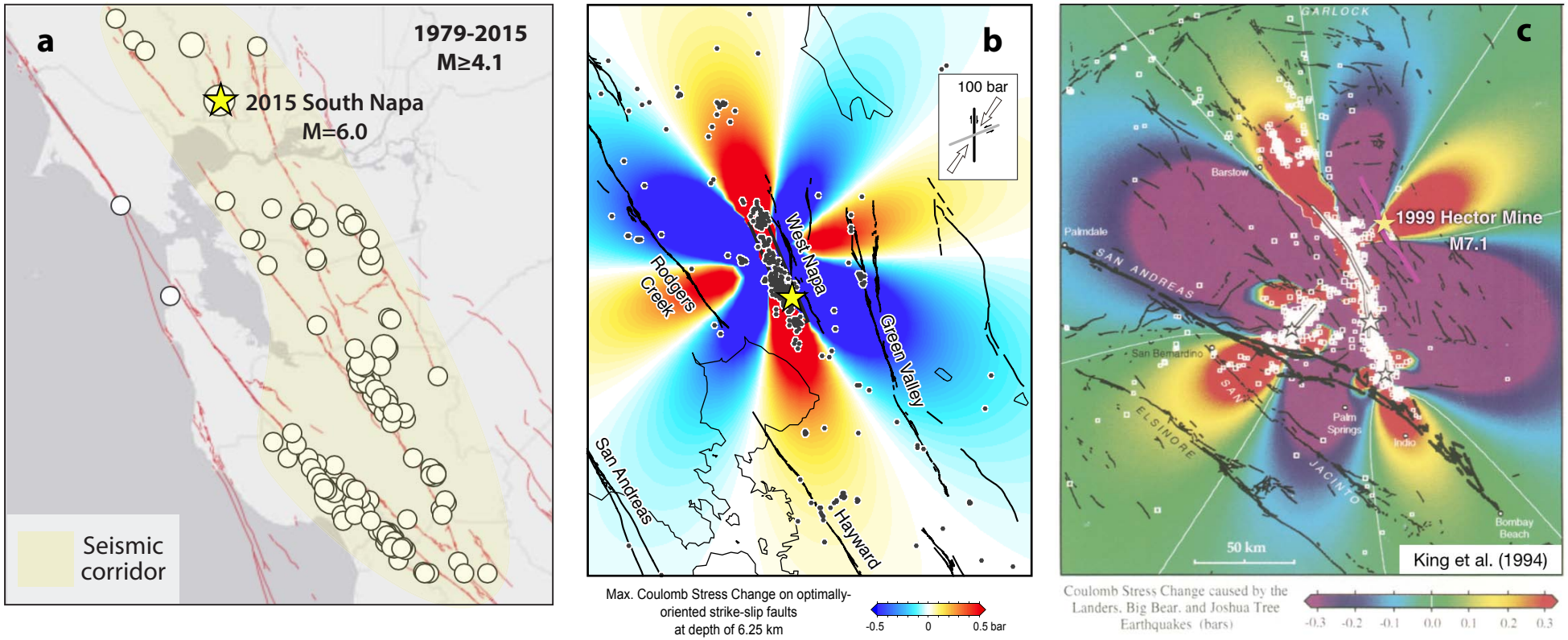

Fig. 1

Toda & Stein

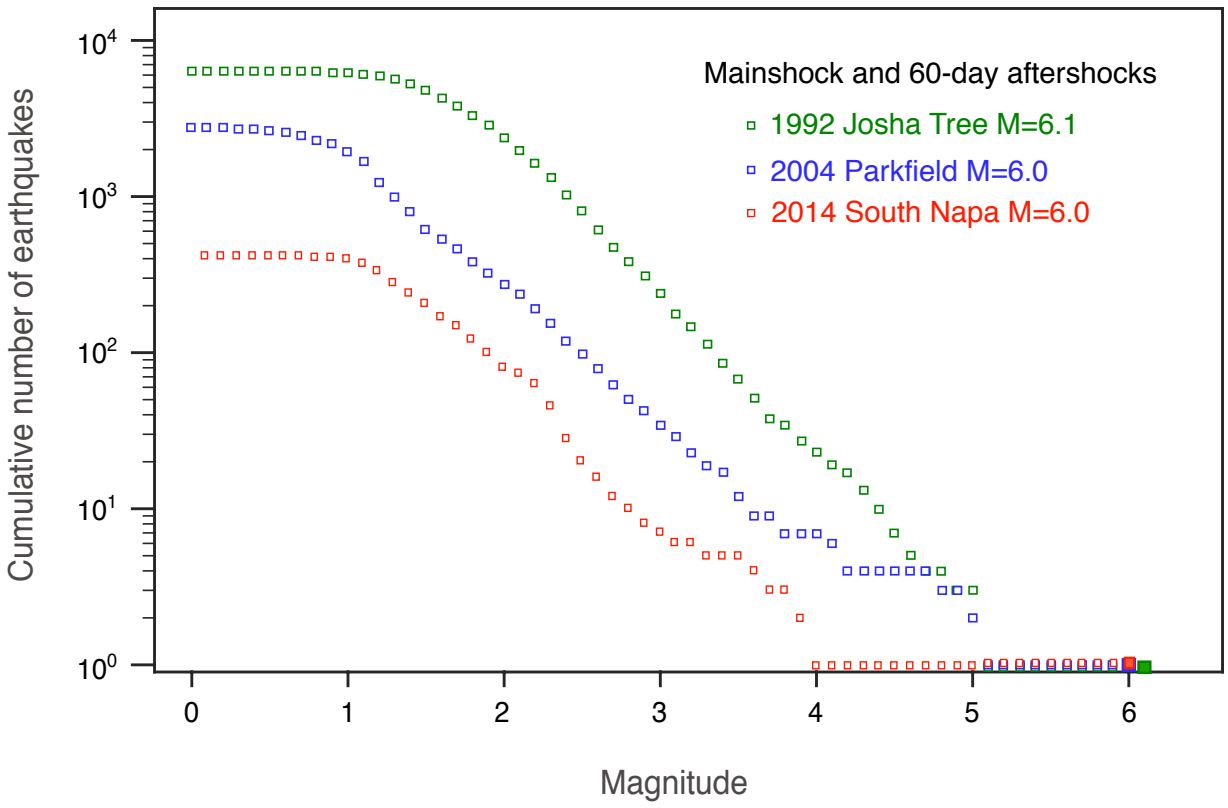

Fig. 2
Toda & Stein

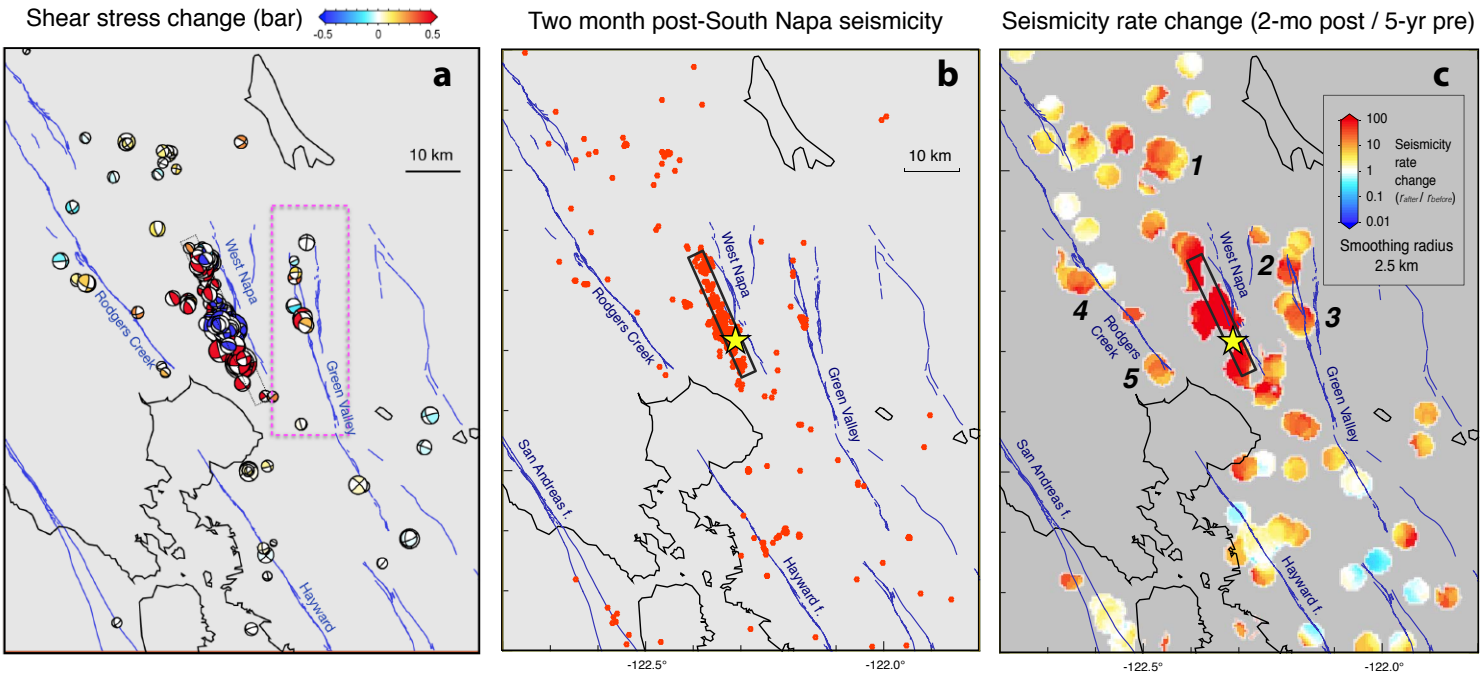

Fig. 3
Toda and Stein

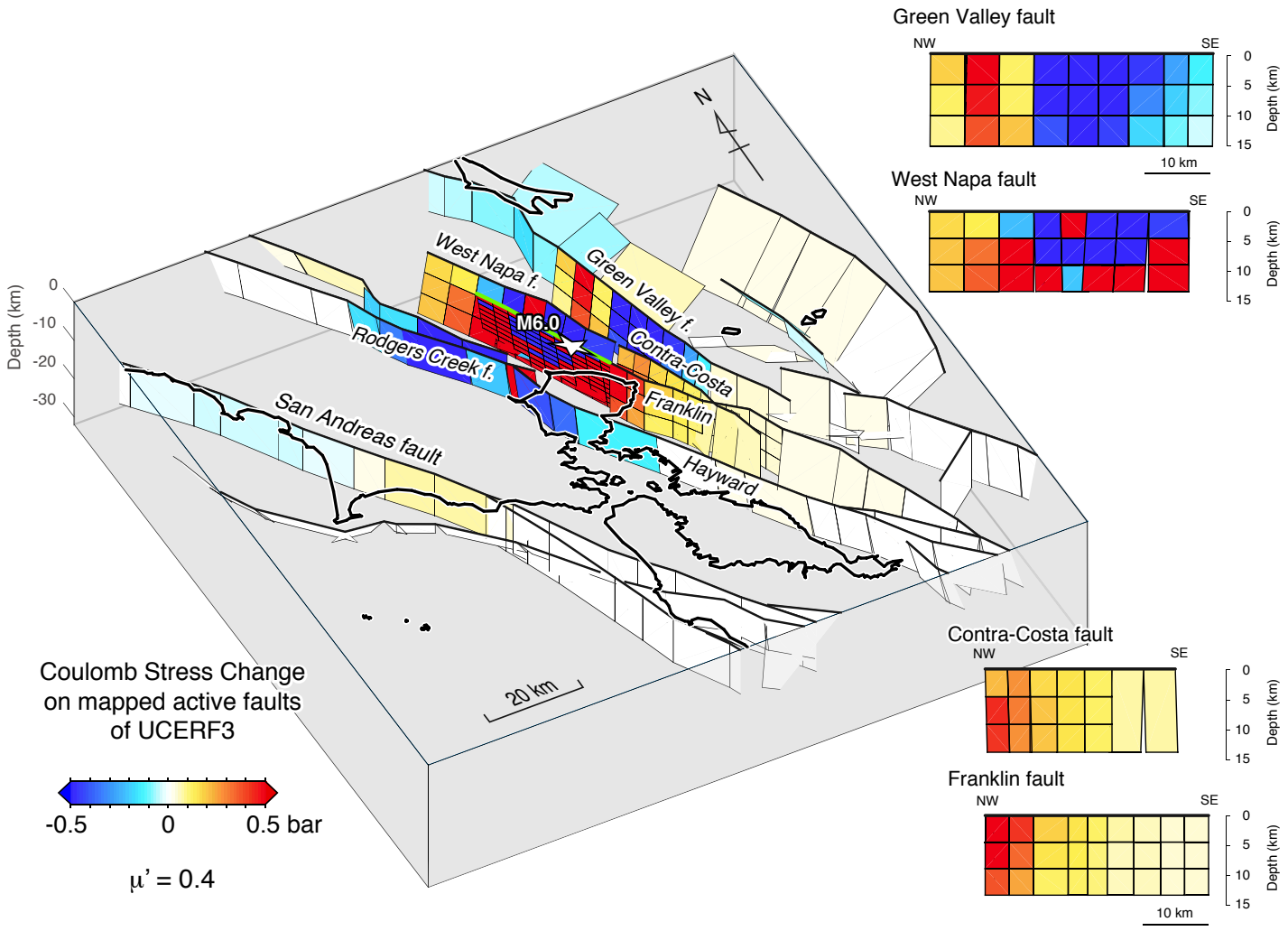

Fig. 4
Toda & Stein

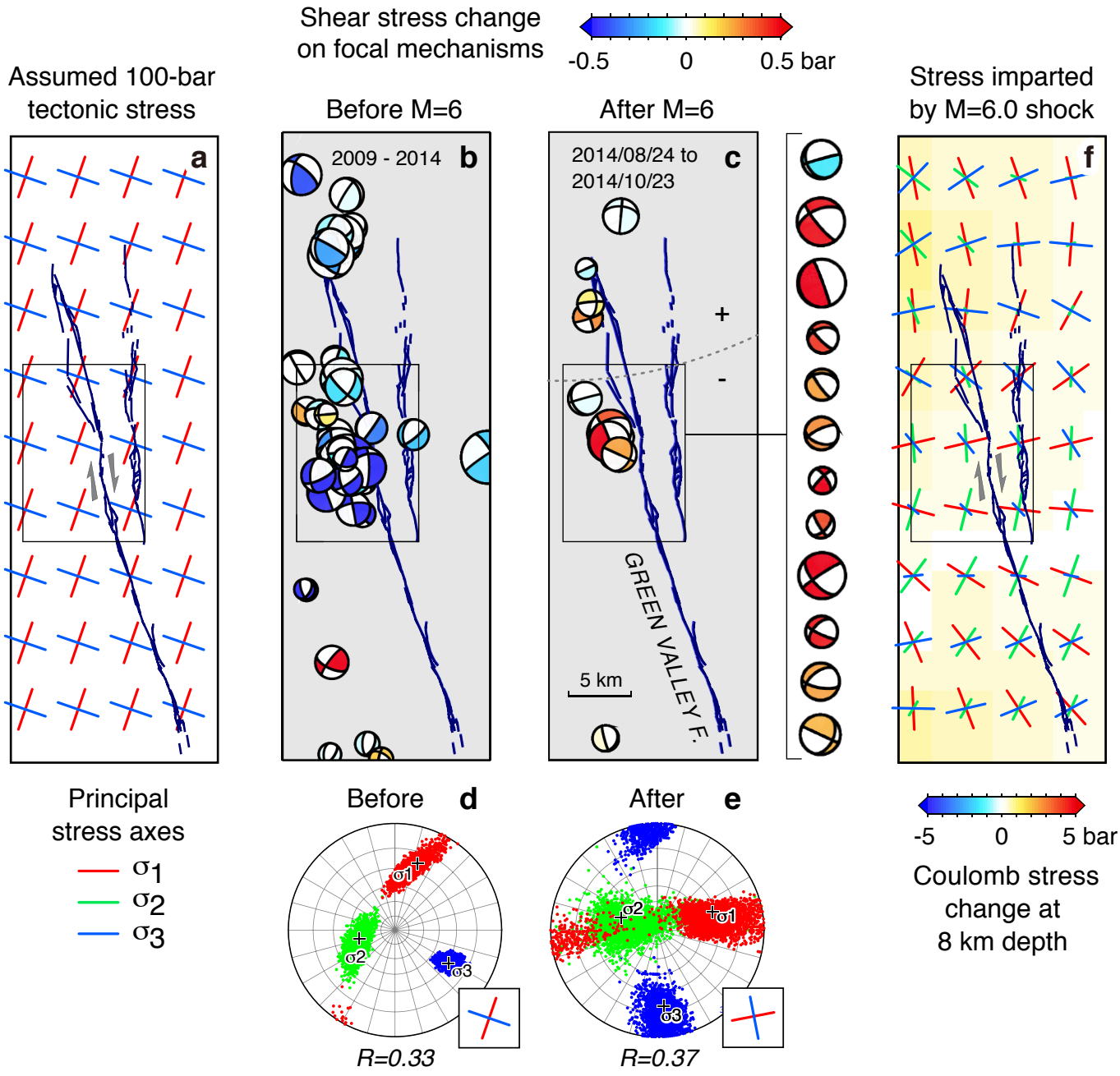

Fig 5
Toda and Stein

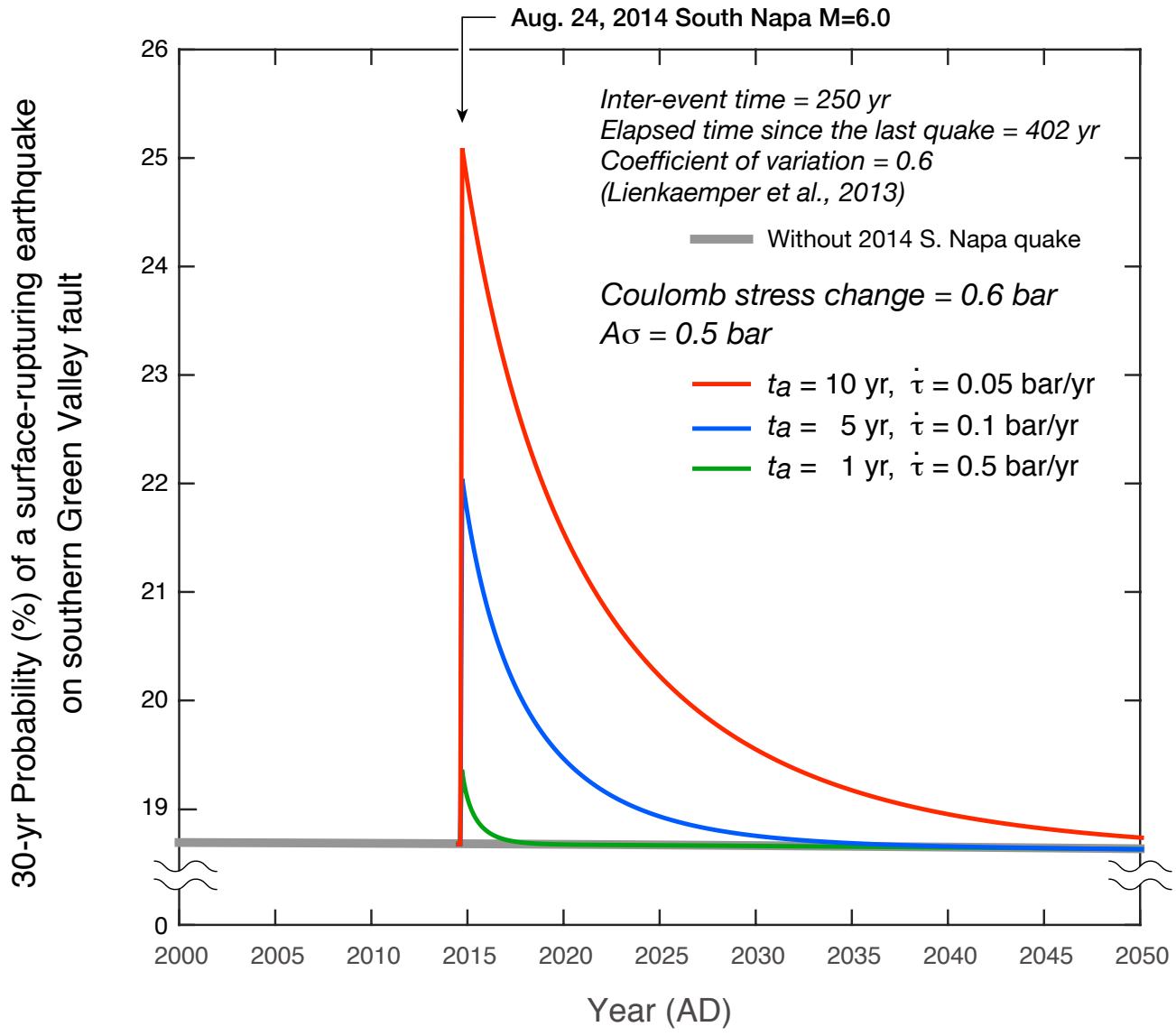

Fig. 6
Toda & Stein

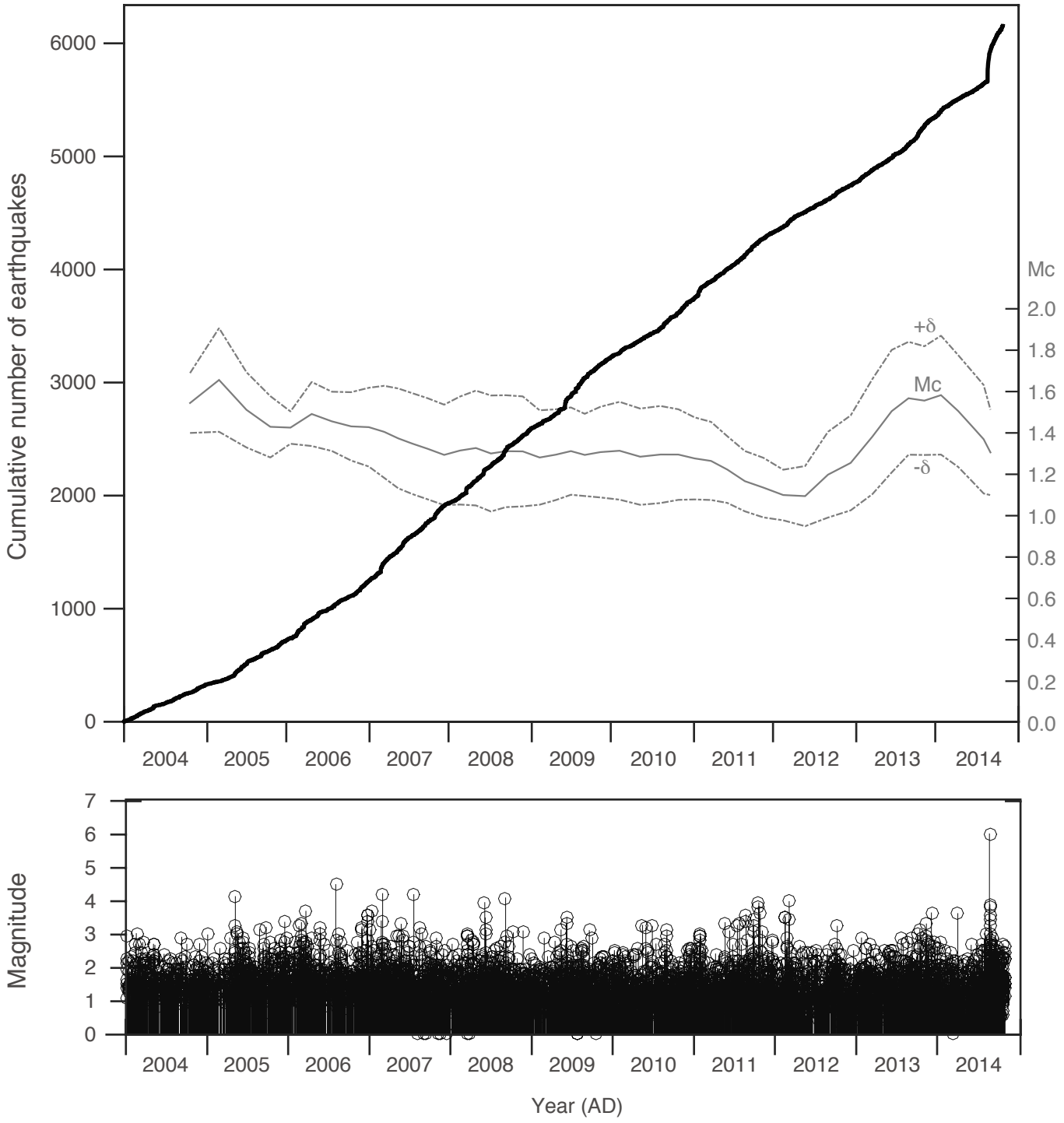
Cumulative number of earthquakes
6000
5000
4000
3000
2000
1000
0
Mc
2.0
1.8
1.6
1.4
1.2
1.0
0.8
0.6
0.4
0.2
0.0
+δ
Mc
-δ
2004
2005
2006
2007
2008
2009
2010
2011
2012
2013
2014
Magnitude
7
6
5
4
3
2
1
0
Year (AD)

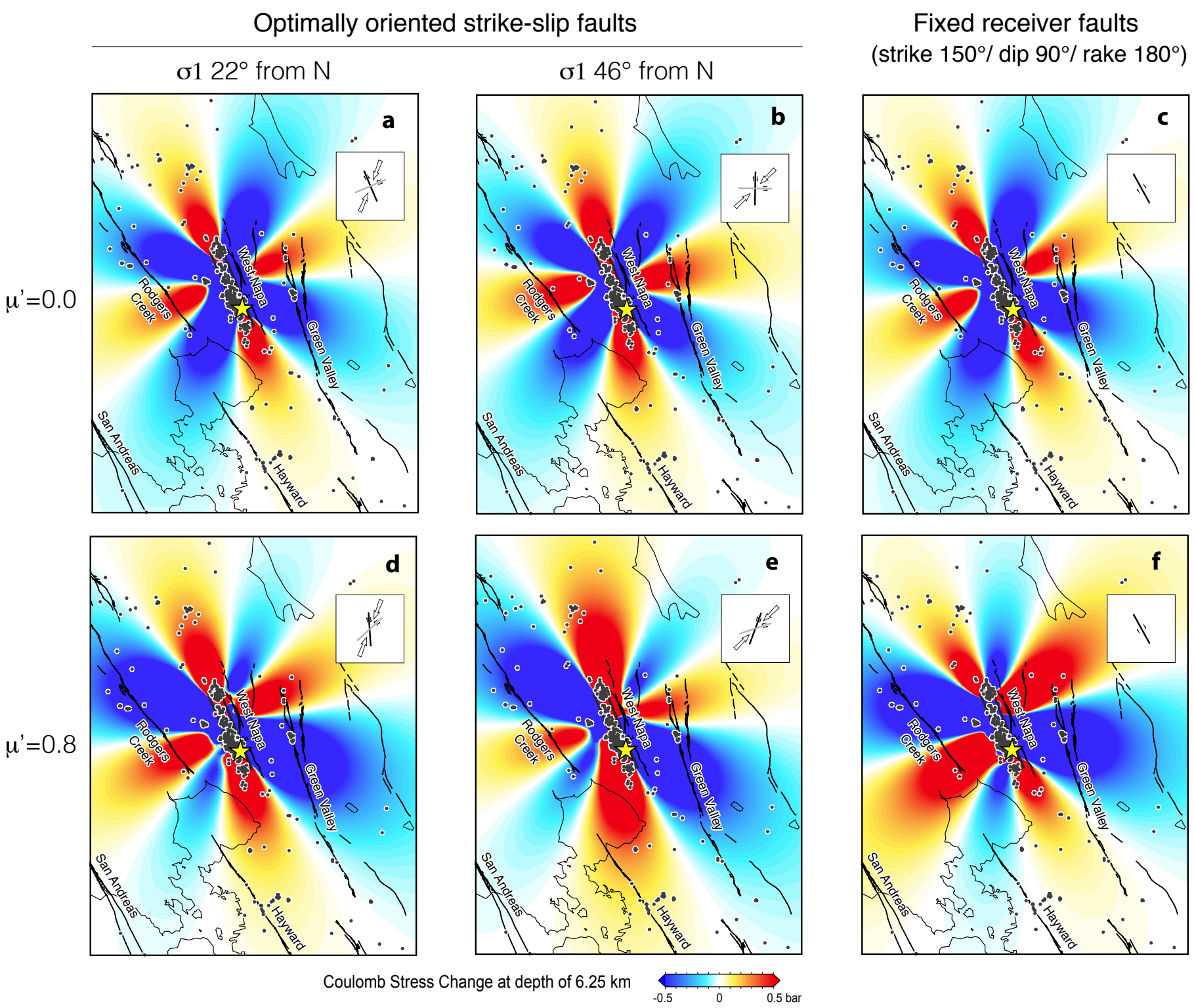
Optimally oriented strike-slip faults
Fixed receiver faults
(strike 150°/ dip 90°/ rake 180°)
σ1 22° from N
σ1 46° from N
μ'=0.0
μ'=0.8
a
b
c
d
e
f
West Napa
Rodgers Creek
Green Valley
San Andreas
Hayward
Coulomb Stress Change at depth of 6.25 km
-0.5
0
0.5 bar

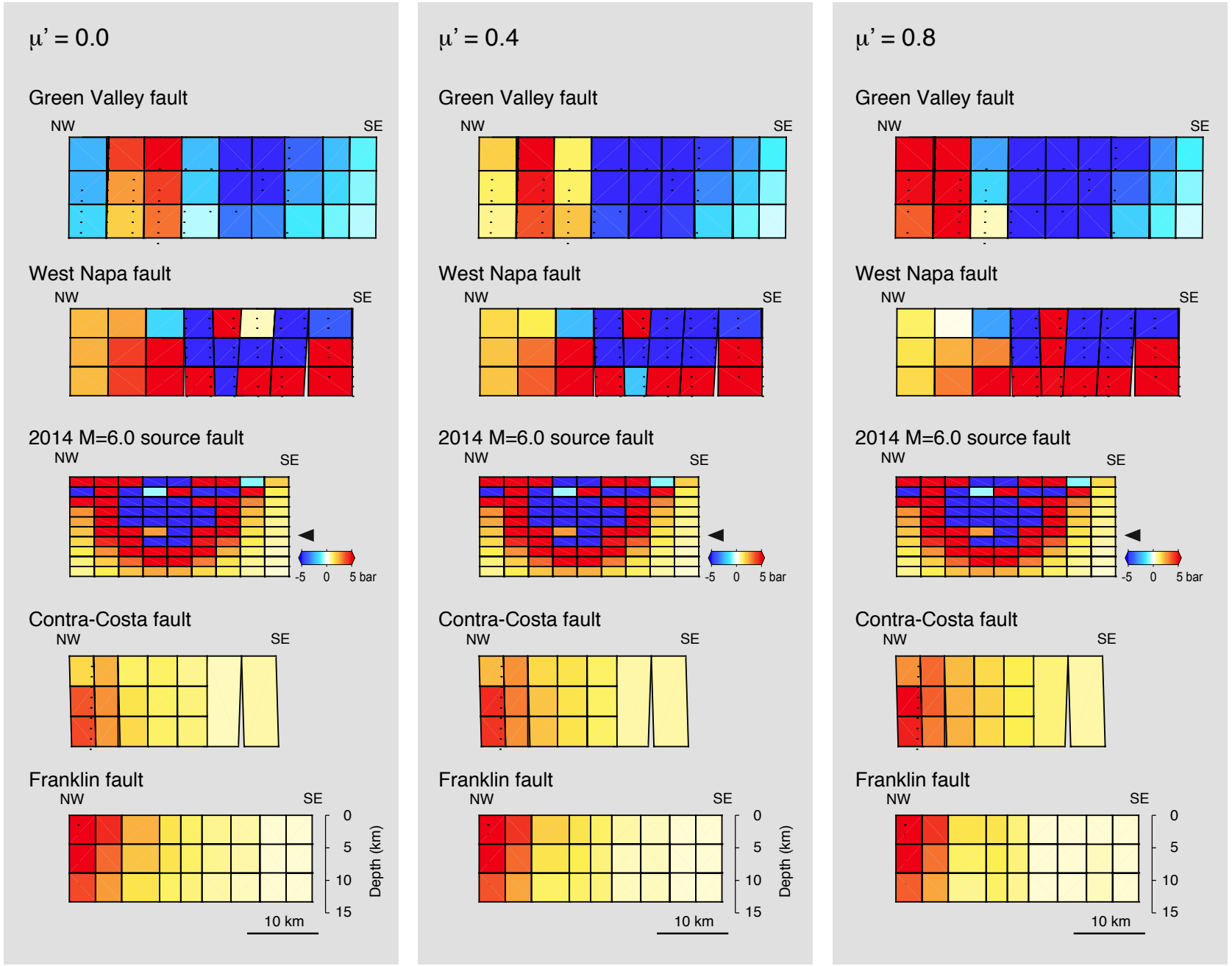
μ' = 0.0
Green Valley fault
NW
SE
West Napa fault
NW
SE
2014 M=6.0 source fault
NW
SE
-5
0
5 bar
Contra-Costa fault
NW
SE
Franklin fault
NW
SE
0
5
10
15
Depth (km)
10 km
μ' = 0.4
Green Valley fault
NW
SE
West Napa fault
NW
SE
2014 M=6.0 source fault
NW
SE
-5
0
5 bar
Contra-Costa fault
NW
SE
Franklin fault
NW
SE
0
5
10
15
Depth (km)
10 km
μ' = 0.8
Green Valley fault
NW
SE
West Napa fault
NW
SE
2014 M=6.0 source fault
NW
SE
-5
0
5 bar
Contra-Costa fault
NW
SE
Franklin fault
NW
SE
0
5
10
15
10 km

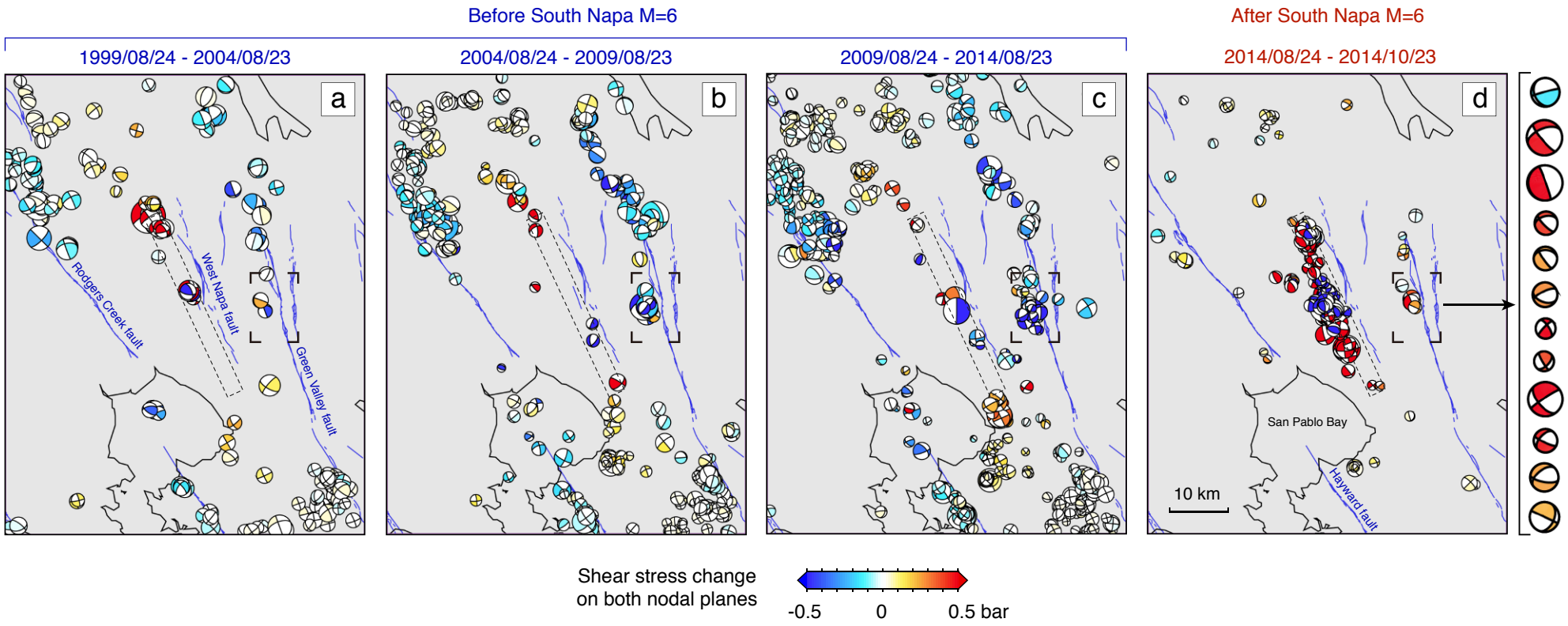
Before South Napa M=6
After South Napa M=6
1999/08/24 - 2004/08/23
2004/08/24 - 2009/08/23
2009/08/24 - 2014/08/23
2014/08/24 - 2014/10/23
a
b
c
d
Rodgers Creek fault
West Napa fault
Green Valley fault
San Pablo Bay
Hayward fault
10 km
Shear stress change
on both nodal planes
-0.5
0
0.5 bar

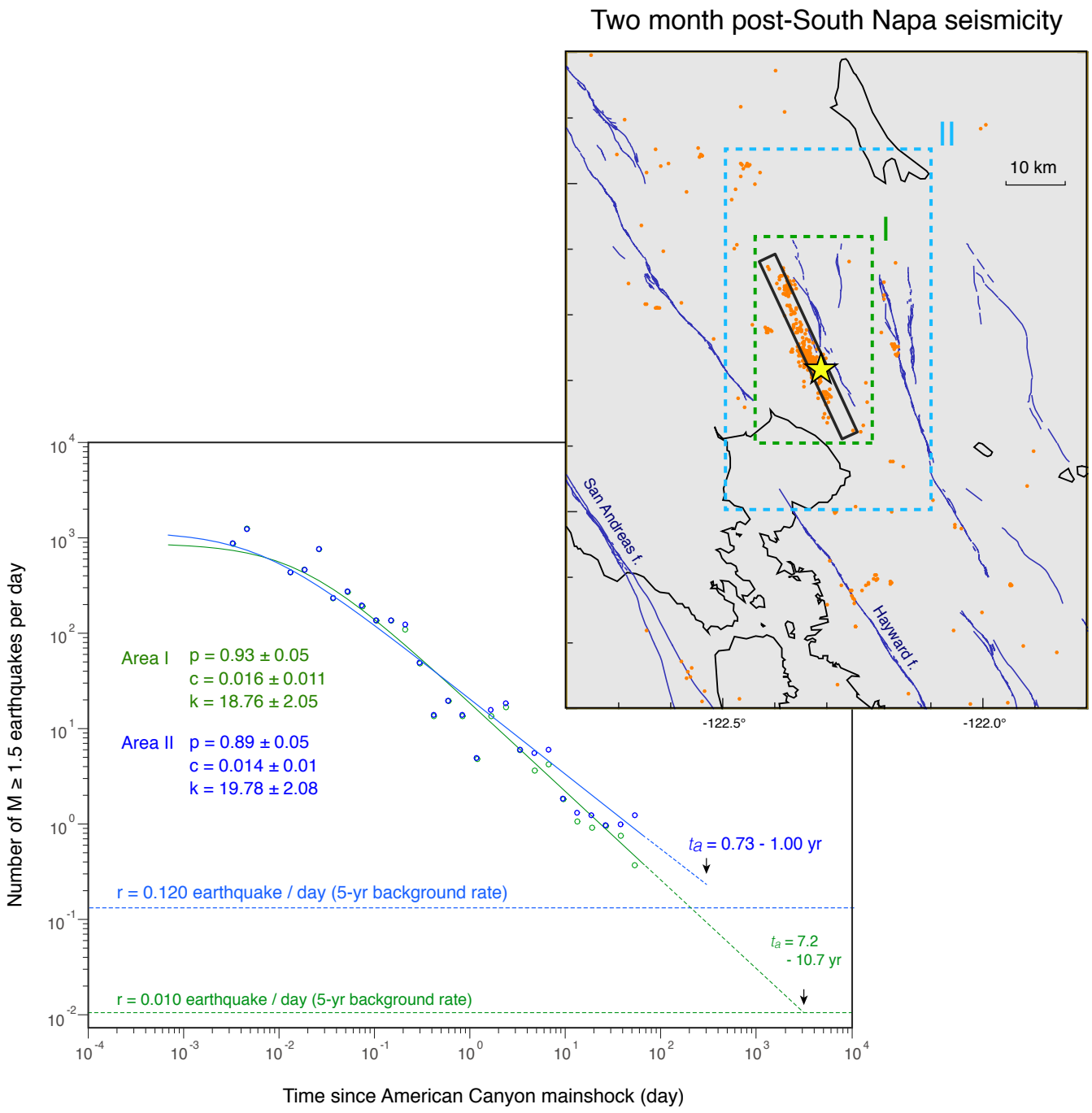
Two month post-South Napa seismicity
10 km
II
I
San Andreas f.
Hayward f.
-122.5°
-122.0°
Area I p = 0.93 ± 0.05
c = 0.016 ± 0.011
k = 18.76 ± 2.05
Area II p = 0.89 ± 0.05
c = 0.014 ± 0.01
k = 19.78 ± 2.08
ta = 0.73 - 1.00 yr
r = 0.120 earthquake / day (5-yr background rate)
ta = 7.2 - 10.7 yr
r = 0.010 earthquake / day (5-yr background rate)
Number of M ≥ 1.5 earthquakes per day
Time since American Canyon mainshock (day)

Electronic Supplement to

2014 M=6.0 South Napa earthquake triggered widespread aftershocks and stressed several major faults and exotic fault clusters by Shinji Toda and Ross S. Stein

These five figures explain further details of our seismicity and stress analyses.

Figure S1. Cumulative (a) and interval (b) background seismicity rate and magnitude of completeness, Mc. The slope of the cumulative number of earthquakes has been stable from 2004, with a slightly lower rate after ~2007. The magnitude of completeness (Mc) as a function of time following Woessner and Wiemer (2005) as implemented in the ZMAP software (Wiemer, 2001) is shown with ± 1sigma bounds.

Figure S2. The 95% confidence interval on the principal stress orientation from Townend and Zoback (2004), and on the friction coefficient, are explored for the optimally-oriented Coulomb stress change on strike-slip faults (a, b, d, e), and compared to an assumed fixed fault orientation (c, f).

Figure S3. The influence of fault friction on the Coulomb stress imparted to the major mapped active faults. Note that regardless of friction, portions of the Green Valley fault are brought closer to failure.

Figure S4. Shear stress changes resolved on the nodal planes of small earthquakes that occurred prior to (a-c) and after (d) the 2014 South Napa earthquake, as proxies for the sites of small active faults. Fault plane solutions are from the Northern California Earthquake Data Center (NCEDC, http://ncedc.org/ncedc/catalog-search.html). Color of compressional region on each beach ball indicates amount of stress change. We split the pre-South Napa period into three

sub-periods to avoid overlapping beach balls in the maps. Blue lines are mapped late Quaternary faults.

Figure S5. Observed aftershock rates (dots) as a function of time for the South Napa earthquake, fitted to an Omori-Utsu function (solid line), $N(t)=k/(t+c)^p$. Two areas, I and II in inset map, are applied to the analyses. Together with observed background rates of M≥1.5 as Mc from Fig. S1, we estimate aftershock durations, t_a, for the wider area I and the narrower area II several months and several years respectively.

REFERENCES

Townend, J., and M. D. Zoback (2004). Regional tectonic stress near the San Andreas fault in central and southern California, *Geophys. Res. Lett.*, **31**, L15S11, doi:10.1029/2003GL018918.

Woessner, J., and S. Wiemer (2005). Assessing the quality of earthquake catalogues: Estimating the magnitude of completeness and its uncertainty, *Bull. Seism. Soc. Amer.*, **95**, 684-698.

Wiemer, S. (2001). A software package to analyse seismicity: ZMAP, *Seismol. Res. Lett.*, **72**, 373-382.